Early-Time Observations of the Type Ia Supernova 2020bpi
with the Transiting Exoplanet Survey Satellite

Tyler Barna [ID]

Department of Physics and Astronomy,
Rutgers University, Piscataway, NJ 08854

ABSTRACT

In this thesis, I present analysis of the lightcurve of SN 2020bpi, a Type Ia supernova observed by the Transiting Exoplanet Survey Satellite (TESS). In particular, I have analyzed the lightcurve of SN 2020bpi observed at early-times across two adjacent TESS data sectors in order to determine the possibility of any companion signature. SN 2020bpi is well fit by a power law model with a power law exponent of 1.8 ± 0.1 and an explosion date of 58875.77 ± 0.37 MJD, which corresponds to January 27th 2020 18:29 UT with an uncertainty of roughly 9 hours. Combined with a fit of the supernova lightcurve, I determined a rise time to maximum light of 17.8 ± 0.4 days. This is in line with other normal Type Ia supernovae. This analysis finds no significant evidence of companion emission for SN 2020bpi, and additional analysis should be able to to place an upper limit on the companion radius.

Keywords: Supernovae; Type Ia Supernovae; Astrophysics - High Energy Astrophysical Phenomena

1. INTRODUCTION

Supernovae (SNe) occur at the end of a star's life, during which it undergoes a violent explosion, generating a luminosity of comparable order to the host galaxy; these explosions produce most of the metals present in the universe (Olling et al. 2015). The primary classification system for SNe groups them based on properties of their spectra; Type I SNe demonstrate no hydrogen lines, whereas the spectra of Type II SNe have hydrogen lines present (Minkowski 1941).

Another means of categorizing SNe is by the mechanism through which they occur. Most of the various SN subtypes distinguish between core-collapse explosions of massive stars (Woosley et al. 2002). Here, I focus on the other main class: Type Ia supernovae (SNe Ia).

SNe Ia occur as a result of thermonuclear runaway of a white dwarf star (WD) in a binary system, producing a large explosion that unbinds the star. While almost all of the energy from the initial explosion is converted into kinetic energy, the radioactive decay of nickel-56 reheats the ejecta and produces an observable lightcurve (Jha et al. 2019).

Though there are documented instances of SNe Ia that are notably under-luminous, sometimes referred to as SNe Iax (Foley et al. 2013), most SNe Ia occur for carbon-oxygen WDs of a similar mass and generally follow a well-defined characteristic lightcurve. As a result of SNe Ia generally reaching a consistent peak luminosity, they are often referred to as "standardizable candles" and are used to measure extra-galactic distances (Jha et al. 2019). This feature makes them useful to astronomers, particularly in the area of cosmology. Observations of SNe Ia were a significant factor in the discovery that the expansion of the universe is accelerating. (Riess et al. 1998) and Perlmutter et al. (1999) found that high-redshift SNe Ia were moving away more than would be expected in a decelerating universe; members of these teams were later awarded the Nobel Prize in Physics for this discovery (Nobel Foundation 2011). SNe Ia can also be used to constrain cosmological parameters, the age of the universe, and the equation of state dark energy (Garnavich et al. 1998).

One of the outstanding questions regarding SNe Ia is the exact nature of the progenitor system; while there is strong evidence that suggests they occur as a result of a WD interacting with a companion in a binary system (Kasen 2010), the exact nature of this companion is unknown. There are currently two primary models for SN Ia progenitor systems: the double degenerate (DD) model and the single degenerate (SD) model.

The DD model posits that SNe Ia occur when two WDs merge, producing a super-Chandrasekhar limit WD that then undergoes thermonuclear runaway (Jha et al. 2019). The SD model suggests that SNe

Ia arise from a WD accreting mass from a Main-Sequence companion until it approaches the Chandrasekhar limit[1] (Olling et al. 2015).

In the SD model, ejecta from the exploding WD should collide with the companion star, producing an increase in emission that should be apparent in the lightcurve of the SNe Ia. However, this signature has not yet been definitively detected in observations. This is due to several complicating factors. This emission is predicted to be most significant just a few days after the WD explodes before being overtaken by the rising luminosity of the SN itself (Kasen 2010).

As a result, SNe Ia must be observed both early and often in order to detect companion emission; this is problematic for observing, as it is difficult to identify and observe specific SNe Ia so soon after their explosion. In fact, astronomers did not observe a SN Ia at the time of its explosion until 2008 (Soderberg et al. 2008). Even when a SN Ia can be viewed at the time of its explosion, there are still factors that might obscure companion emission, such as if the WD is in front of the companion when the explosion occurs. In order to meaningfully study this phenomenon, a catalog of SNe Ia observed at early times must be compiled.

In recent years, the scope of surveys has significantly increased, with a number of all-sky surveys that are currently ongoing or seeing first light in the near future, such as the Legacy Survey of Space and Time (LSST) at the Vera C. Rubin Observatory (Ivezić et al. 2019). Untargeted all-sky surveys are a potential avenue through which companion emission can be studied, as they should provide a large number of potential SN Ia targets observed at various wavelengths both before and after their explosion.

1.1. TESS

TESS was launched in 2018 as a Medium-Class Mission for the NASA Explorers Program, serving as somewhat of a successor to the Kepler Space Telescope, which was deactivated that same year. The two-year primary mission was conducted from 2018–2020 with the goal of identifying exoplanets orbiting nearby stars (Ricker et al. 2015).

TESS is outfitted with four cameras that cover a combined $24° \times 90°$ area of the sky. TESS observes in the optical and near-infrared, with the TESS band defined

as having a wavelength range of $600 - 1000$ nm. Observations are divided into sectors, each lasting for two orbits of the telescope, or roughly 27 days (Ricker et al. 2015). TESS is notable for being the first all-sky exoplanet survey conducted with a space telescope; its predecessor, the Kepler Space Telescope, surveyed around 0.25% of the sky (Borucki et al. 2010).

During the TESS Primary Mission, the telescope imaged approximately 85% of the night sky over the course of two years and 26 sectors, observing the southern hemisphere in the first year and the northern hemisphere in the second (Ricker et al. 2015). This resulted in over 2,200 new exoplanet candidates, several of which have already been confirmed (Guerrero et al. 2021; Huang et al. 2018; Wang et al. 2019; Dragomir et al. 2019; Huber et al. 2019). Additionally, the TESS Input Catalog (TIC) has recorded over one million unique targets observed by TESS in full frame images (FFIs) at a 30 minute cadence and roughly 200,000 candidate target list (CTL) members observed in postage stamps at a two minute cadence (Stassun et al. 2018).

1.2. SN 2020bpi

SN 2020bpi is a low redshift SNe Ia ($z = 0.041$) that was first detected by the Zwicky Transient Facility (ZTF) (Bellm et al. 2019; Graham et al. 2019) on January 30th, 2020 (Hiramatsu et al. 2020). Serendipitously, SN 2020bpi was also observed by TESS in two adjacent sectors, Sector 21 (S21) and Sector 22 (S22)[2], which took place from January 21st to February 18th and February 19th to March 17th, respectively; SN 2020bpi is observed by TESS from before its explosion to well after its peak.

The primary motivation behind analyzing SN 2020bpi specifically is the fact that is a target for The Supernovae in the Infrared avec Hubble (SIRAH) Program. SIRAH is an ongoing program led by Professor Saurabh Jha that observes SNe Ia just after their peak, making use of both the Hubble Space Telescope (HST) and the Keck Observatory in Hawaii among other instruments (Jha et al. 2020). In contrast, this thesis analyzes the early times of SN 2020bpi to search for companion emission.

2. DATA REDUCTION

Like Kepler, TESS was designed for exoplanet detection but also demonstrates potential for studying other objects, including SNe Ia (Soares-Furtado et al. 2020; Shappee et al. 2019). Each TESS sector images roughly

---

[1] The current consensus among astronomers is that the WD never actually reaches the Chandrasekhar limit; rather, it approaches the limit before undergoing a period of convection followed by fusion triggered by an as-yet undetermined mechanism.

[2] SN 2020bpi was observed with TESS Camera 3 for both sectors but was observed with CCD2 for S21 and CCD1 for S22.
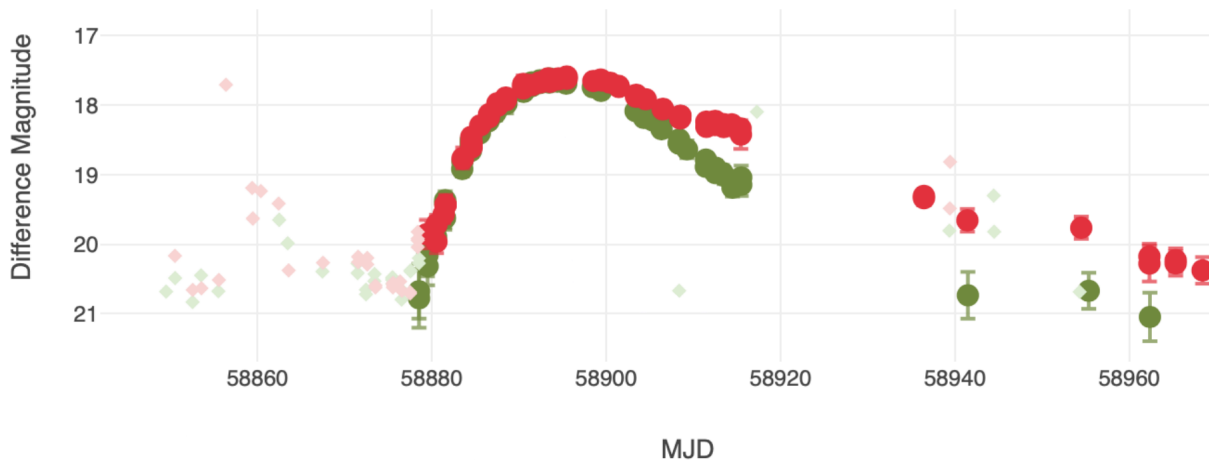
Figure 1. The ZTF lightcurve of 2020bpi from Lasair (Smith et al. 2019). The green points are observations in the g-band and the red points are observations in the r-band. Diamond points represent non-detections.

5% of the night sky at any given time, which increases the chance of serendipitous viewing of SNe Ia at the time of their explosion; however, this comes at the cost of resolution. TESS pixels are notably large, covering about 21" per pixel (Ricker et al. 2015). Compare this to HST, an instrument frequently used to study SNe Ia (Freedman et al. 1999; Jha et al. 2020), which has a resolution of roughly 0.1" (Kimble et al. 2008). Due to this, SN Ia observations with TESS are limited by the reduced contrast relative to the background flux in the pixel.

TESS was placed into a highly elliptical orbit to minimize the interference of Earthshine, another consequence of the large field of view. As a result, the data at the beginning and end of each orbit is rendered unusable due to the telescope passing close to earth for data transmission, lasting roughly a day. Each sector takes place over two TESS orbits, so there is a gap of roughly a day in the middle of each sector (Ricker et al. 2015). This is acceptable for exoplanets with a transit duration of less than ~ 13.7 days, but it could make fitting a Se Ia lightcurve difficult if the explosion happened to occur at or near this transmission gap. However, this did not appear to be the case for SN 2020bpi.

Another consideration is the availability of data reduction tools for TESS optimized for SNe. I initially attempted to use `eleanor`, a python library for analysis of TIC objects with aperture photometry (Feinstein et al. 2019)[3], but the built-in background subtraction methods were not designed with SN lightcurves in mind, so a great deal of SN light was subtracted.

---

[3] My analysis also made frequent use of `astropy` (Astropy Collaboration et al. 2013, 2018)

This is because exoplanet transits occur on much shorter timescales than SNe.

As a consequence of its nature as a telescope made for surveying exoplanets, TESS observes objects at a cadence much higher than most SN-specific surveys. This is useful for attempting to observe companion emission, as the signature is only detectable for a few days in optical wavelengths (Kasen 2010). As a result, some astronomers have explored using TESS for studying SN Ia companions, including Dr. Michael Fausnaugh at the MIT Kavli Institute, who developed a TESS background subtraction pipeline (hereafter referred to as the Fausnaugh pipeline) specifically for SNe (Fausnaugh et al. 2021). Dr. Fausnaugh has collaborated with Professor Jha in the past, and after reaching out to him with a list of SIRAH targets and other interesting SNe Ia observed by TESS, he provided me with data from his pipeline. My analysis of SN 2020bpi is based on data from his pipeline.

2.1. Image Subtraction

Fausnaugh et al. (2021) explains the image subtraction method in further detail, but, in short, the Fausnaugh pipeline retrieves data from the Transient Name Server (TNS) to identify targets and then applies the image subtraction method defined in Alard (2000) and Alard & Lupton (1998), constructing a median stacked image of the relevant FFIs as a reference that is then used to subtract out background light and systematic errors after transforming and convolving the FFI in question.

The Fausnaugh pipeline produces a much clearer lightcurve for SN 2020bpi, but there are still some considerations that must be made. The Fausnaugh pipeline was not able to remove all of the scattered light from
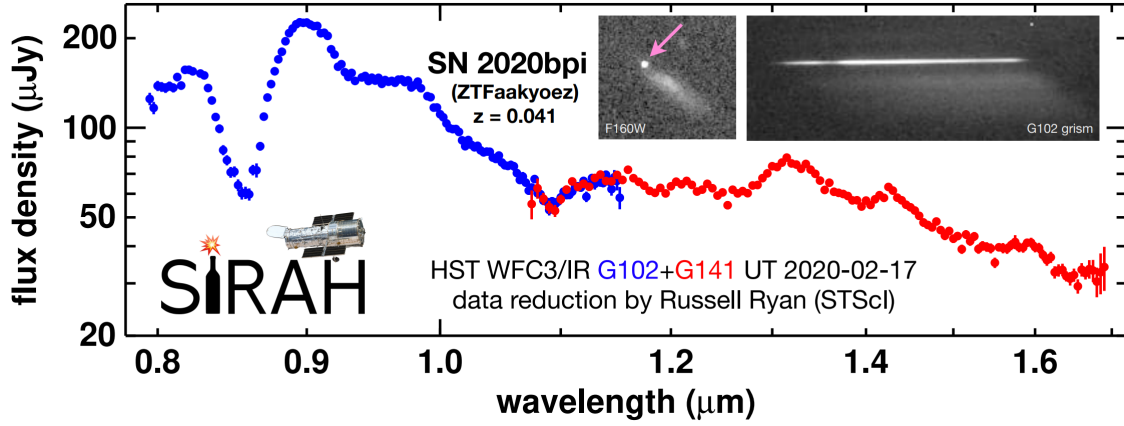
Figure 2. Hubble Space Telescope near-infrared spectrum of SN 2020bpi taken near peak luminosity by the SIRAH collaboration. The insets show an infrared image of the supernova and its wavelength-dispersed light.

the times near the beginning of each orbit. As a result, the first day of S21 data is excluded from the analysis in order to prevent the model fitting from being affected, though this still leaves several days of observation of the SN 2020bpi progenitor prior to the first ZTF detection. There is some amount of excess Earthshine for a small number of data points following the start of the second orbit in S21, but this data is left in for the analysis, as increasing the size of the gap in the lightcurve had a more adverse effect on the fit than excluding the data at the start.

The initial version of the S22 data provided by Dr. Fausnaugh was affected by a known issue with some of the TESS CCDs that create "stripes" of pixels with artificially increased responses; this was fixed in a later version of the data. That being said, S21 was the primary dataset used for this analysis.

2.2. Lightcurve Normalization

The raw counts and corresponding errors from the data were converted into a pseudo-flux by applying the following function

$$flux = \frac{counts}{T_{TESS} A_{TESS}} \tag{1}$$

where the average exposure time is taken to be $T_{TESS} \sim 2010.8$ s and the detector area is taken as $A_{TESS} \sim 86.6$ cm^2 (Ricker et al. 2015).

2.2.1. Correction of TESS Lightcurve with ZTF

In an attempt to further correct the TESS lightcurve, I explored adjusting the lightcurve processed by the Fausnaugh pipeline using contemporaneous observations from ZTF. Following the first detection of SN 2020bpi by ZTF in the g-band on the night of January 30, 2020, SN 2020bpi was observed an additional 31 times in that

band before the lightcurve reached its peak. The first detection in the r-band occurred on January 31, 2020, and SN 2020bpi was observed an additional 29 times before it reached its peak magnitude.

ZTF observes in three primary bands: the g-band ($408.67 - 552.20$ nm), the r-band ($560.04 - 731.67$ nm), and the i-band ($702.71 - 888.37$ nm) (Masci et al. 2019). However, i-band data is not released to the public. Additionally, the ZTF g-band was not used for this analysis because it observes in a range outside of the TESS band.

While the ZTF r-band has a wavelength range that lies within the TESS band, it does not encompass the entire TESS-band, meaning TESS will observe light at frequencies that the ZTF r-band cannot. For the purposes of this analysis, the ZTF data was analyzed as given and band discrepancies were not accounted for; this is one source of systematic uncertainty that could be quantified and mitigated in future analysis.

To correct the lightcurve, I maximize a likelihood function of the model using a Markov Chain Monte Carlo (MCMC) method from the `emcee` python package.

The likelihood function is given by

$$\ln\left(p\left(\Phi_{\text{ZTF}}|\phi, s\right)\right) = \tag{2}$$
$$-\frac{1}{2}\sum_i \ln\left(2\pi s_i^2\right) + \frac{\left(\Phi_{\text{ZTF},i} - \phi_i\right)^2}{s_i^2}$$

The model ϕ is given by

$$\phi\left(\Phi_{\text{TESS}}, \beta_{\text{TESS}}\right) = C\Phi_{\text{TESS}} + \phi_0 - D\beta_{\text{TESS}} \tag{3}$$

where Φ_{TESS} and β_{TESS} are the flux and background in the TESS data, C and D are scaling factors, and ϕ_0 is a constant zero-point. The variance is
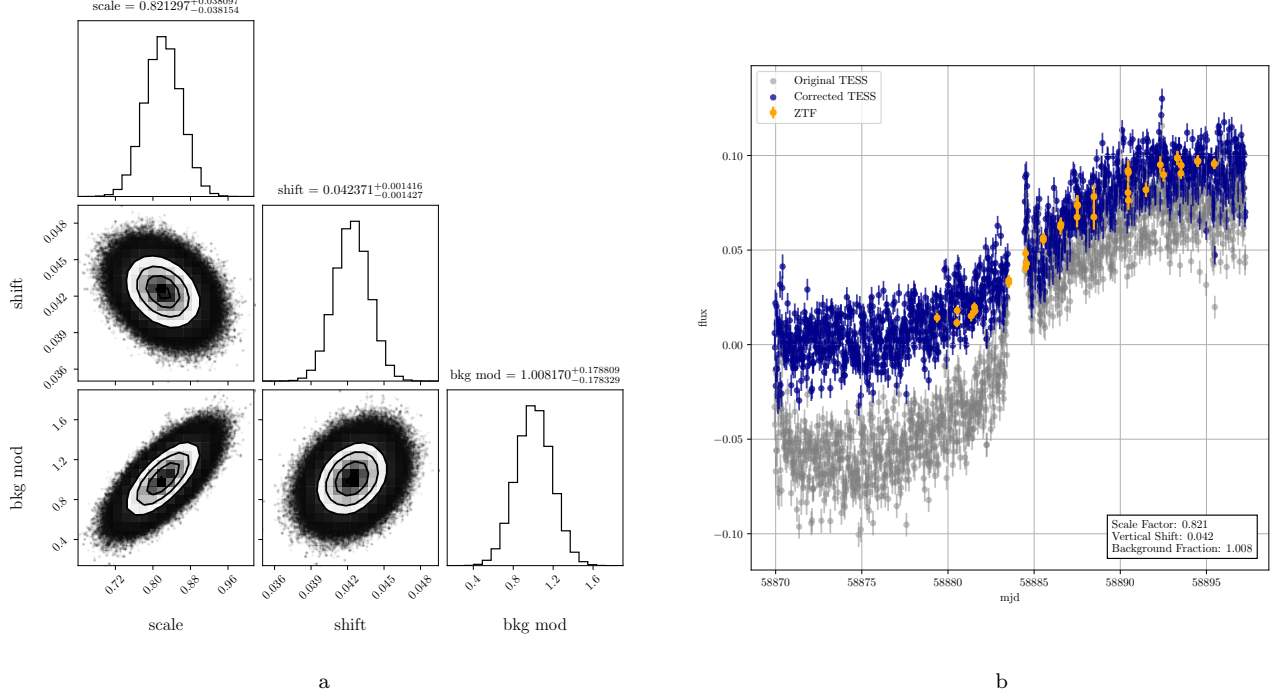
$$s^2 = \sigma_{\text{TESS}}^2 \tag{4}$$

Figure 3. Fitting of the TESS lightcurve to the ZTF lightcurve based on the model shown in Equation 3. Figure 3a represents a corner plot of the MCMC analysis and Figure 3b compares the original and adjusted TESS lightcurves.

The results of these corrections can be seen in Figure 3. This results in a TESS lightcurve that corresponds closely to the ZTF lightcurve. However, for reasons that are not yet entirely understood, this process biased additional lightcurve modeling, so we chose to analyze the uncorrected TESS lightcurve in the subsequent analysis.

3. LIGHTCURVE ANALYSIS

Prior research has shown that the early rise of SNe Ia are well-fit by a basic power-law model; Olling et al. (2015) suggests that fitting the lightcurve up to the point at which it reaches 40% of its peak provides the best fit. For SN 2002bpi, this cutoff occurs at approximately 58887 MJD. This is 17 days into Sector 21 of the TESS data; this is shortly after the data transmission gap, which lasted from 58883.5 MJD to 58884.5 MJD.

Once again, I make use of `emcee` to maximize a likelihood function through Markov Chain Monte Carlo analysis. To limit the degeneracy between model parameters, the flux is normalized to 40% of the 12 hour rolling median peak flux and adjusted to an appropriate zero-point.

3.1. *Power Law Fitting*

The likelihood function used to model the power law is similar to Equation 2; it is given by

$$\ln\left(p\left(\Phi_{\text{TESS}}|\phi,s\right)\right) = \qquad (5)$$
$$-\frac{1}{2}\sum_i \ln\left(2\pi s_i^2\right) + \frac{\left(\Phi_{\text{TESS},i} - \phi_i\right)^2}{s_i^2}$$

To reduce the degeneracy between the power and multiplicative constant, the model ϕ is expressed as

$$\phi\left(t\right) = \begin{cases} y_0 & t \le t_0 \\ A\left(\frac{t-t_0}{t_{40}-t_0}\right)^\alpha + y_0 & t > t_0 \end{cases} \qquad (6)$$

where the primary parameters of interest are t_0, which is the Ia SNe explosion time, and α, which is the power law exponent. A and y_0 parameterize the normalization and zero-point; they are included as nuisance parameters so their uncertainties propagate to the parameters of interest. The constant t_{40} is the time at which the 12 hour rolling median of the flux exceeds 40% of the peak.

The variance is given by

$$s^2 = \sigma_{\text{TESS}}^2 + \sigma^2 \qquad (7)$$

where σ is an additional inherent scatter parameter included to allow for any unmodeled uncertainty in the TESS photometry; however, I found this was unnecessary in the ultimate analysis and therefore set $\sigma = 0$.
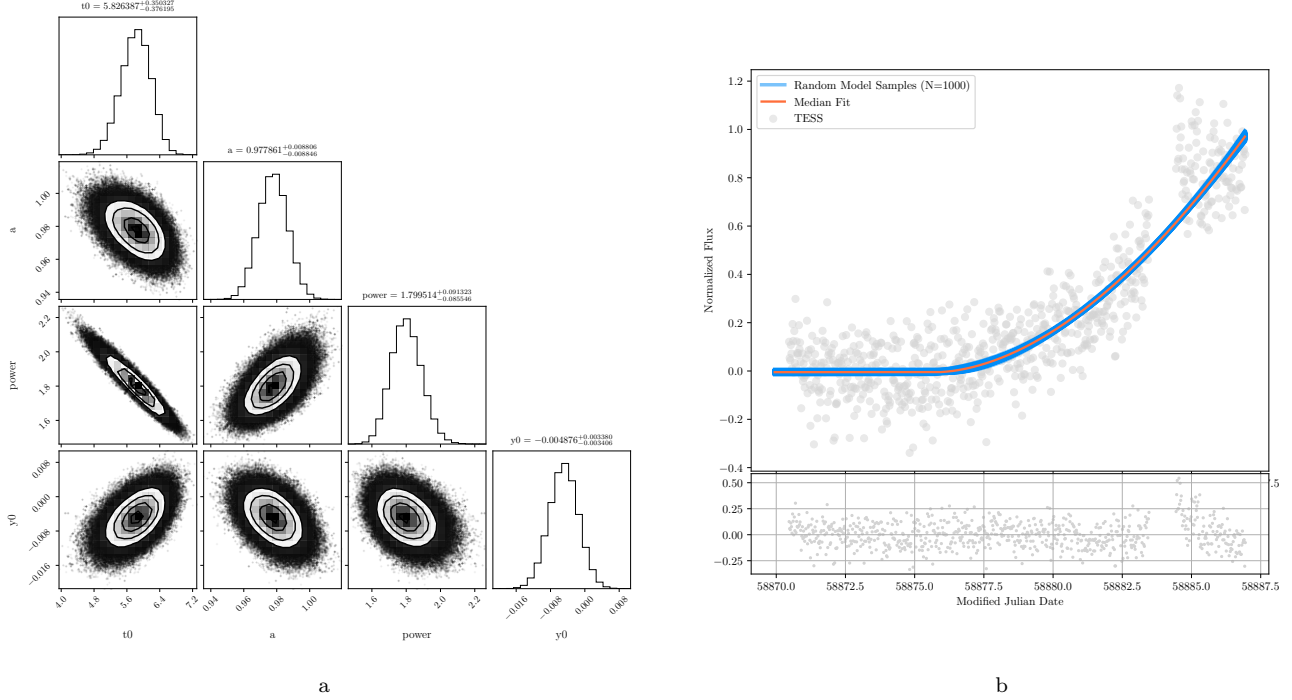
Figure 4. A MCMC fit of the TESS lightcurve using the model used in Equation 6. Figure 4a shows a corner plot of the parameters for Equation 6. In Figure 4b, the blue lines show random samples from the MCMC analysis, with the orange line representing the best fit. The residuals of the best fit are shown in the lower subplot; the increased residuals just after the data gap are likely the result of an increased background due to Earthshine, though this is fortunately well after the time after the time of explosion.

Figure 4a shows this fit as applied to the TESS SN 2020bpi lightcurve, and Figure 4b is the corner plot of the previously mentioned parameters. The best model predicts that SN 2020bpi exploded on 58875.77 ± 0.37 MJD, which roughly corresponds to January 27th, 2020. This suggests SN 2020bpi exploded around 3 days prior to the first detection by ZTF. Additionally, I found the power law exponent to be $\alpha = 1.8 \pm 0.1$. This is also within expectations for SNe Ia, which are usually found to have power law exponents ranging from $\sim 1.5 - 2.5$ (Miller et al. 2020).

Based on the MLCS2k2 SN Ia lightcurve fitting method Jha et al. (2007), the peak of the lightcurve occurred at 58894.30 ± 0.13 MJD. To account for cosmological time dilation, the following equation is used to calculate the rise time

$$t_{\rm rise} = \frac{t_{\rm peak} - t_0}{1 + z} \qquad (8)$$

I found the rise time of SN 2020bpi to be 17.8 ± 0.4 days. This agrees with the results of similar analyses; (Miller et al. 2020) found an average rise time of 17.9 ± 1.8 days for a large sample of ZTF objects.

Running the same analysis on the ZTF lightcurve of SN 2020bpi highlighted the effect of having observations directly before, during, and after the expected explosion time. The ZTF lightcurve predicts a similar explosion date of 58875.97 ± 3.75 MJD. Once again using Equation 8, I found the ZTF lightcurve predicts a rise time of 17.6 ± 3.6 days. One should note the statistical uncertainty of these values, which are roughly an order of magnitude larger than those of the TESS lightcurve. The power law exponent of the ZTF data was found to be $\alpha = 2.29 \pm 0.77$. This is consistent with the TESS power law exponent but is again less precise. That the larger power law exponent translates to a shorter time to peak also suggests this may be a result of degeneracy with the explosion time, which is poorly constrained by the ZTF data. Overall, the ZTF data alone is unable to constrain the power law model to the same precision as the TESS lightcurve, demonstrating the advantage of having more frequently sampled data both before and after the explosion. That being said, there are several ZTF non-detections of SN 2020bpi from prior to the TESS-estimated explosion, so it might be possible to further constrain these parameters with ZTF by using those data points, taking into consideration that they may not have the same accuracy as ZTF detections.

3.1.1. *Companion Emission*

Kasen (2010) describes the emission expected from the interaction of SN ejecta with binary companion stars of differing radii. In section 5 of Fausnaugh et al. (2021), the authors perform the necessary calculations to find the flux in units of electrons per second for the TESS band for companions of $0.1R_\odot$, $0.5R_\odot$, $1R_\odot$, $5R_\odot$, $10R_\odot$, $25R_\odot$, and $50R_\odot$. The companion emission data from Fausnaugh et al. (2021) is given for a system observed at a distance of 100 Mpc. In order to apply this to SN 2020bpi, this must be converted to the proper distance.

The luminosity distance is given by

$$F = \frac{L}{4\pi D_L^2} \qquad (9)$$

Hubble's Law is defined as

$$v = H_0 d \qquad (10)$$

For objects of sufficiently low redshift, such as SN 2020bpi, Equation 10 can be approximated as

$$d \approx \frac{cz}{H_0} \qquad (11)$$

Taking $H_0 = 72.8$ km s^{-1} Mpc^{-1} (Dhawan et al. 2018), I find that $d_{2020\mathrm{bpi}} \approx 174.2$ Mpc.

Therefore, the conversion of the companion flux to the distance of SN 2020bpi is

$$F_z = \left(\frac{100 \text{ Mpc}}{174.2 \text{ Mpc}} \right)^2 F_{100\mathrm{Mpc}} \qquad (12)$$

where $F_{100 \text{ Mpc}}$ is the companion emission flux as given in Fausnaugh et al. (2021) and the redshift of SN 2020bpi is $z = 0.041$. This is in units of electrons per second, so it is also divided by A_{TESS} to match the units of Equation 1.

I applied the same normalization factor to the companion emission as I did the SN 2020bpi data, and the resulting emission signatures are shown in Figure 5.

Figure 6 shows the companion emission signatures as compared to the residual values of the best power law fit for SN 2020bpi. If companion emission is present, the residual values of the fit at times greater than t_0 should roughly correspond to the companion emission models.

However, there is no strong emission demonstrated in the residuals. Barring some significant systematic error in the MCMC fit, the $10R_\odot$, $25R_\odot$, and $50R_\odot$ companion models can be easily ruled out given that they exceed the residual flux.
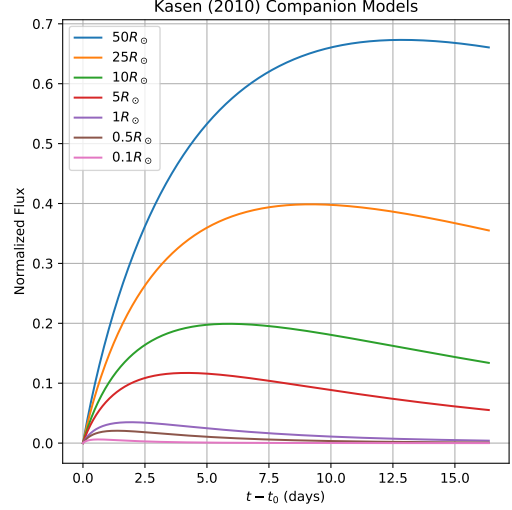

Figure 5. The companion models from Fausnaugh et al. (2021) scaled to the distance of SN 2020bpi.

3.1.2. *Companion Radius as a Parameter*

A more precise method of constraining the radius of the companion would be to include the companion radius as a parameter in the MCMC model; this would also have the benefit of providing statistical uncertainties for all parameters that take into account possible companion emission. While the code for the MCMC modeling of the lightcurves is written in such a way to make adding new parameters and models easy, making a model based off the Fausnaugh et al. (2021) companion flux requires a number of additional operations, and this model was not in a satisfactory state at the time of this writing[4].

I had planned on performing a linear interpolation of the Fausnaugh et al. (2021) companion flux depending on the companion radius before interpolating to match the times observed by TESS. However, the model from Kasen (2010) does not have a linear dependence on radius, and a linear interpolation might not be entirely accurate for constraining the radius.

Ultimately, the ideal power law model would include the parameters used to calculate the companion emission from Kasen (2010). That being said, the residuals of the SN 2020bpi TESS data fit demonstrate no significant trend with the Fausnaugh et al. (2021) companion

---

[4] Though I do plan on completing this model and experimenting with other more exotic models, such as the two component power law model used in Shappee et al. (2019)
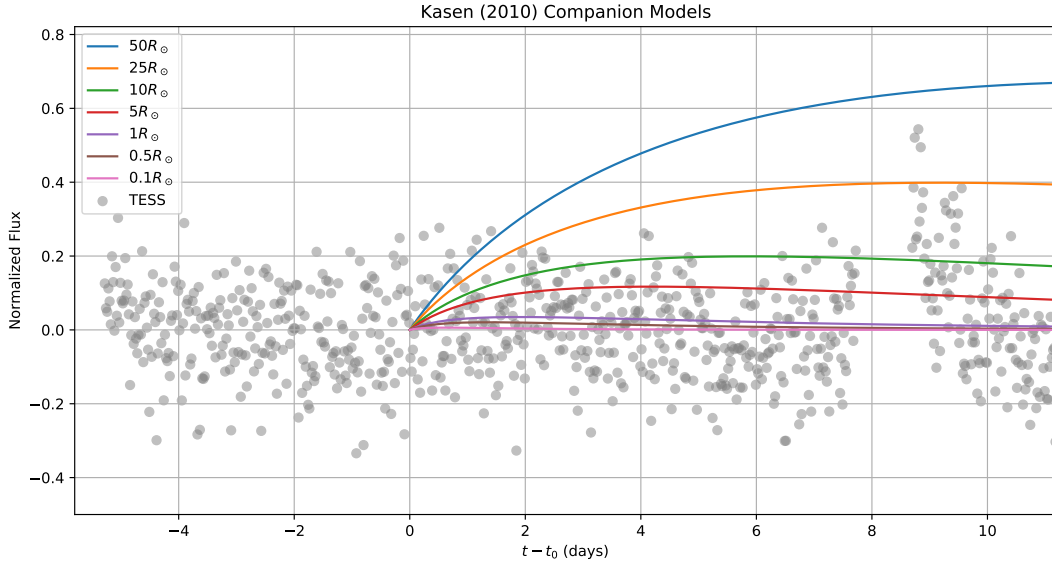
Figure 6. The scaled emission models from Fausnaugh et al. (2021) as compared to the residuals of Figure 4b. Models with radii above $5R_\odot$ exceed the residual, suggesting the companion has a radius below this value.

flux models, and all radii above $5R_\odot$ are unlikely provided the underlying model is sound.

4. CONCLUSIONS

I find that the early TESS lightcurve of the SN Ia 2020bpi is well modeled by a power law as predicted by previous literature. The TESS lightcurve demonstrates a rise with a power law exponent of $\alpha = 1.8 \pm 0.1$ and an explosion date of 58875.77 ± 0.37 MJD. This result implies that TESS observed the explosion of SN 2020bpi roughly a quarter of the way through TESS S21, several days before ZTF had its first detection.

While there is still work to be done in order to more confidently constrain an upper limit on the radius of the companion star for SN 2020bpi, this analysis finds no significant evidence for companion emission, suggesting that the companion is likely less than $5M_\odot$. Though this analysis somewhat constrains the radius of the companion, it does not rule out a SD progenitor system. With a more complex MCMC model, I will be able to make use of models from Kasen (2010) and establish an uncertainty for the companion radius that takes into account other model parameters in the same fit.

Additionally, the methods used for this thesis can be applied to other SIRAH targets and SNe Ia observed by TESS and ZTF. With a larger number of samples, it will be possible to more reliably constrain an upper limit on companion radii. Recent work has suggested that SNe Ia may actually arise out of a mix of both DD and SD progenitor systems, underscoring the importance of a large sample of well-observed SNe Ia when studying companion emission.

After TESS concluded its two-year primary mission, funding was granted for an additional two-year extended mission that is currently ongoing. During this mission, TESS will provide further coverage of the sky and revisit targets of interest for follow-up observations. Furthermore, the cadence for full-frame observations has been increased from every 30 minutes to every 10 minutes, further improving the sampling of future targets. During this extended mission, an even greater number of SNe Ia will be viewed, which will provide valuable data on the nature of SNe Ia progenitor systems.

REFERENCES

Alard, C. 2000, A&AS, 144, 363, doi: 10.1051/aas:2000214

Alard, C., & Lupton, R. H. 1998, The Astrophysical Journal, 503, 325, doi: 10.1086/305984

Astropy Collaboration, Robitaille, T. P., Tollerud, E. J., et al. 2013, A&A, 558, A33, doi: 10.1051/0004-6361/201322068

Astropy Collaboration, Price-Whelan, A. M., Sipőcz, B. M., et al. 2018, AJ, 156, 123, doi: 10.3847/1538-3881/aabc4f

Bellm, E. C., Kulkarni, S. R., Graham, M. J., et al. 2019, PASP, 131, 018002, doi: 10.1088/1538-3873/aaecbe

Borucki, W. J., Koch, D., Basri, G., et al. 2010, Science, 327, 977, doi: 10.1126/science.1185402

Dhawan, S., Jha, S. W., & Leibundgut, B. 2018, A&A, 609, A72, doi: 10.1051/0004-6361/201731501

Dragomir, D., Teske, J., Günther, M. N., et al. 2019, ApJL, 875, L7, doi: 10.3847/2041-8213/ab12ed

Fausnaugh, M. M., Vallely, P. J., Kochanek, C. S., et al. 2021, ApJ, 908, 51, doi: 10.3847/1538-4357/abcd42

Feinstein, A. D., Montet, B. T., Foreman-Mackey, D., et al. 2019, PASP, 131, 094502, doi: 10.1088/1538-3873/ab291c

Foley, R. J., Challis, P. J., Chornock, R., et al. 2013, ApJ, 767, 57, doi: 10.1088/0004-637X/767/1/57

Freedman, W. L., Mould, J. R., Kennicutt, R. C., J., & Madore, B. F. 1999, in Cosmological Parameters and the Evolution of the Universe, ed. K. Sato, Vol. 183, 17. https://arxiv.org/abs/astro-ph/9801080

Garnavich, P. M., Jha, S., Challis, P., et al. 1998, ApJ, 509, 74, doi: 10.1086/306495

Graham, M. J., Kulkarni, S. R., Bellm, E. C., et al. 2019, PASP, 131, 078001, doi: 10.1088/1538-3873/ab006c

Guerrero, N. M., Seager, S., Huang, C. X., et al. 2021, arXiv e-prints, arXiv:2103.12538. https://arxiv.org/abs/2103.12538

Hiramatsu, D., Hosseinzadeh, G., Jha, S. W., et al. 2020, Transient Name Server Classification Report, 2020-390, 1

Huang, C. X., Burt, J., Vanderburg, A., et al. 2018, ApJL, 868, L39, doi: 10.3847/2041-8213/aaef91

Huber, D., Chaplin, W. J., Chontos, A., et al. 2019, AJ, 157, 245, doi: 10.3847/1538-3881/ab1488

Ivezić, Ž., Kahn, S. M., Tyson, J. A., et al. 2019, ApJ, 873, 111, doi: 10.3847/1538-4357/ab042c

Jha, S., Riess, A. G., & Kirshner, R. P. 2007, ApJ, 659, 122, doi: 10.1086/512054

Jha, S. W., Maguire, K., & Sullivan, M. 2019, Nature Astronomy, 3, 706, doi: 10.1038/s41550-019-0858-0

Jha, S. W., Avelino, A., Burns, C., et al. 2020, Supernovae in the Infrared avec Hubble, HST Proposal

Kasen, D. 2010, ApJ, 708, 1025, doi: 10.1088/0004-637X/708/2/1025

Kimble, R. A., MacKenty, J. W., O'Connell, R. W., & Townsend, J. A. 2008, in Society of Photo-Optical Instrumentation Engineers (SPIE) Conference Series, Vol. 7010, Space Telescopes and Instrumentation 2008: Optical, Infrared, and Millimeter, ed. J. Oschmann, Jacobus M., M. W. M. de Graauw, & H. A. MacEwen, 70101E, doi: 10.1117/12.789581

Masci, F. J., Laher, R. R., Rusholme, B., et al. 2019, PASP, 131, 018003, doi: 10.1088/1538-3873/aae8ac

Miller, A. A., Yao, Y., Bulla, M., et al. 2020, ApJ, 902, 47, doi: 10.3847/1538-4357/abb13b

Minkowski, R. 1941, PASP, 53, 224, doi: 10.1086/125315

Nobel Foundation. 2011, The Nobel Prize in Physics 2011. https://www.nobelprize.org/prizes/physics/2011/summary/

Olling, R. P., Mushotzky, R., Shaya, E. J., et al. 2015, Nature, 521, 332, doi: 10.1038/nature14455

Perlmutter, S., Aldering, G., Goldhaber, G., et al. 1999, ApJ, 517, 565, doi: 10.1086/307221

Ricker, G. R., Winn, J. N., Vanderspek, R., et al. 2015, Journal of Astronomical Telescopes, Instruments, and Systems, 1, 014003, doi: 10.1117/1.JATIS.1.1.014003

Riess, A. G., Filippenko, A. V., Challis, P., et al. 1998, AJ, 116, 1009, doi: 10.1086/300499

Shappee, B. J., Holoien, T. W. S., Drout, M. R., et al. 2019, ApJ, 870, 13, doi: 10.3847/1538-4357/aaec79

Smith, K. W., Williams, R. D., Young, D. R., et al. 2019, Research Notes of the American Astronomical Society, 3, 26, doi: 10.3847/2515-5172/ab020f

Soares-Furtado, M., Hartman, J. D., Bhatti, W., et al. 2020, ApJS, 246, 15, doi: 10.3847/1538-4365/ab5fcf

Soderberg, A. M., Berger, E., Page, K. L., et al. 2008, Nature, 453, 469, doi: 10.1038/nature06997

Stassun, K. G., Oelkers, R. J., Pepper, J., et al. 2018, AJ, 156, 102, doi: 10.3847/1538-3881/aad050

Wang, S., Jones, M., Shporer, A., et al. 2019, AJ, 157, 51, doi: 10.3847/1538-3881/aaf1b7

Woosley, S. E., Heger, A., & Weaver, T. A. 2002, Reviews of Modern Physics, 74, 1015, doi: 10.1103/RevModPhys.74.1015